Article
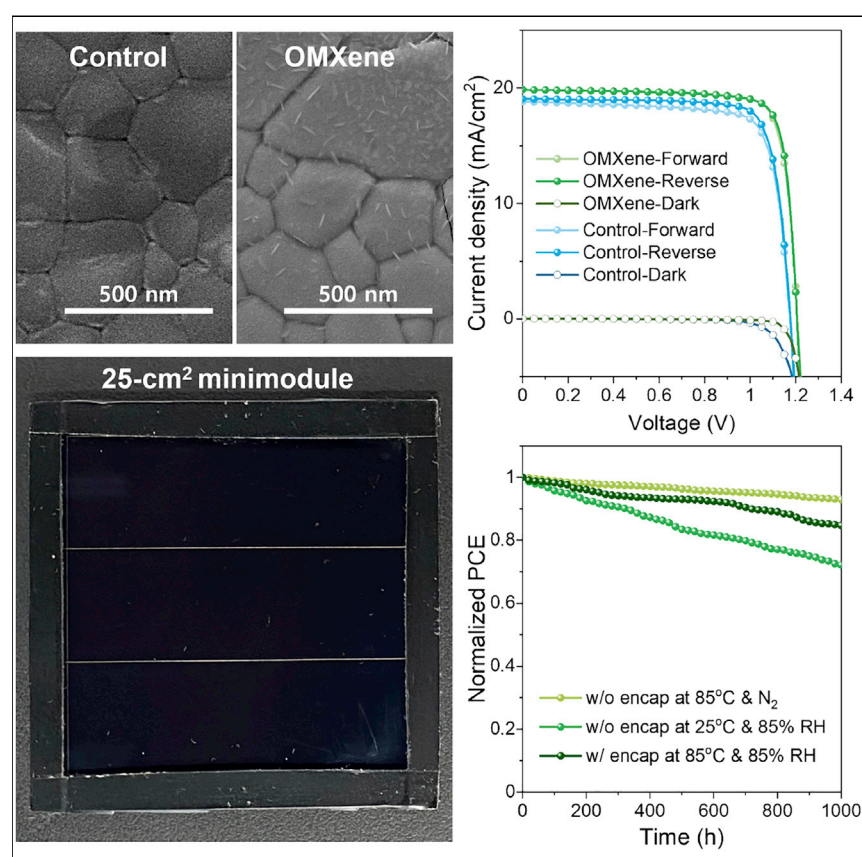
Surface engineering with oxidized $Ti_3C_2T_x$ MXene enables efficient and stable p-i-n-structured $CsPbI_3$ perovskite solar cells

Jin Hyuck Heo, Fei Zhang, Jin Kyoung Park, ..., Joseph J. Berry, Kai Zhu, Sang Hyuk Im

kai.zhu@nrel.gov (K.Z.)
imromy@korea.ac.kr (S.H.I.)

Highlights

Surface engineering of the $CsPbI_3$ layer using oxidized MXene (OM-Xene) is reported

OMXene surface treatment improves the efficiency and stability of the device

Efficiencies of 19.69% for 0.096-cm^2 and 14.64% for 25-cm^2 devices are obtained

The 25-cm^2 minimodule shows good stability under high humidity, heat, and light

Surface engineering of the $CsPbI_3$ perovskite layer with oxidized MXene (OMXene) nanoplates via orthogonal spray coatings is reported. The OMXene surface treatment provides a physical barrier against moisture for the $CsPbI_3$ perovskite layer and also improves charge separation from an enhanced electric field at the perovskite/electron transporting layer interface. With this approach, we obtained power conversion efficiencies of 19.69% for a 0.096-cm^2 cell and 14.64% for a 25-cm^2 minimodule with good stability under high humidity, temperature, and illumination.

Joule

CellPress

Article

Surface engineering with oxidized Ti$_3$C$_2$T$_x$ MXene enables efficient and stable p-i-n-structured CsPbI$_3$ perovskite solar cells

Jin Hyuck Heo,[1,2,5] Fei Zhang,[2,5,6] Jin Kyoung Park,[1] Hyong Joon Lee,[1] David Sunghwan Lee,[1] Su Jeong Heo,[3] Joseph M. Luther,[2] Joseph J. Berry,[3,4] Kai Zhu,[2,*] and Sang Hyuk Im[1,7,*]

SUMMARY

All-inorganic CsPbI$_3$ perovskite has a near-ideal band gap, high thermal stability, and simple material composition, thus presenting a promising option for developing perovskite/Si tandem solar cells. However, CsPbI$_3$ undergoes a rapid phase transition under exposure to moisture and exhibits a significant performance gap relative to other perovskite compounds, particularly in the p-i-n structure favored for perovskite/Si tandems. Here, we demonstrate highly efficient and stable p-i-n-structured CsPbI$_3$ perovskite solar cells by surface engineering the CsPbI$_3$ layer with oxidized Ti$_3$C$_2$T$_x$ MXene (OMXene) nanoplates via spray coatings. OMXene provides a physical barrier against moisture and improves charge separation at the perovskite-electron transporting layer interface via an enhanced electric field. Consequently, we demonstrated CsPbI$_3$/OMXene-based p-i-n devices with efficiencies of 19.69% for 0.096-cm^2 cells and 14.64% for 25-cm^2 minimodules. The encapsulated minimodule showed good stability, retaining ~85% of the initial efficiency under simultaneous damp heat (85°C/85% relative humidity) and 1-sun light soaking for over 1,000 h.

INTRODUCTION

Metal halide perovskites have been of great interest because of their unique properties, such as their high absorption coefficients, small exciton binding energies, ambipolar charge transport, convenient band-gap tunability, and solution processability. The interest in metal halide perovskites began when Kojima et al. reported on liquid junction CH$_3$NH$_3$PbX$_3$ (MAPbX$_3$, X = halogen)-sensitized solar cells.[1] Due to intensive studies on the development of highly efficient perovskite solar cells (PSCs), the record power conversion efficiencies (PCEs) of single-junction PSCs and perovskite/Si two-terminal tandem solar cells have reached 25.5% and 29.5%, respectively.[2] The single-junction PSCs with high PCEs have been demonstrated by organic-inorganic hybrid perovskites with mixed cations (e.g., methylammonium [MA]/formamidinium [FA]/alkali metals) and/or mixed anions (e.g., I/Br), which typically have lower thermal budgets for processing and appear to have more film-level thermal and photostability challenges relative to inorganic perovskites.[3–6] Inorganic perovskites, such as CsPbI$_{3-x}$Br$_x$ (x = 0–1), generally exhibit good thermal stability across a range of wide band gaps (~1.65–1.92 eV), as detailed elsewhere.[7–12] Accordingly, inorganic perovskites are strong candidates for thermally stable single-junction solar cells or for the top cells of efficient perovskite/Si tandem solar cells.

Context & scale

All-inorganic CsPbI$_3$ perovskite is problematic with respect to the rapid phase transition under moisture exposure and exhibits significant performance gaps compared with other perovskite compounds. Here, we report the surface engineering of the CsPbI$_3$ perovskite layer with oxidized MXene (OMXene) nanoplates via orthogonal spray coatings. OMXene surface engineering not only offers a protective barrier against moisture for the CsPbI$_3$ perovskite layer but also enhances charge separation from a strong electric field at the perovskite/electron transporting layer interface. With this approach, we demonstrated a highly efficient and stable p-i-n-structured CsPbI$_3$-based perovskite solar cells with efficiencies of 19.69% for 0.096-cm^2 cell and 14.64% for 25-cm^2 minimodule. In addition, the encapsulated 25-cm^2 minimodules exhibited good stability under simultaneous damp heat (85°C/85% RH) and 1-sun light soaking for over 1,000 h.

Most works on all-inorganic CsPbI$_{3-x}$Br$_x$ PSC development have focused on n-i-p structures, using various strategies such as adduct solution growth, nanostructure/quantum dots, contact layers, graded absorber layers, additive growth, and surface treatment.[13–25] The highest PCE reported so far for a n-i-p-structured CsPbI$_3$ PSC is 21.0%.[26] However, for the development of efficient perovskite/Si tandem solar cells, especially with a two-terminal configuration, efficient and stable p-i-n-structured PSCs are favored, owing to their compatibility on integration with the Si bottom cells.[27–37] In addition, p-i-n-type PSCs are often more stable than n-i-p-type PSCs, which often involve the use of hygroscopic dopants. Nonetheless, the effort to develop p-i-n-structured CsPbI$_x$Br$_{3-x}$ PSCs has significantly lagged behind the development of their n-i-p counterparts.[38–41] Although CsPbI$_{3-x}$Br$_x$ is known to be thermally stable, its moisture stability is inherently weak, and it easily undergoes a phase transition from the photoactive black phase to the nonactive yellow (delta) phase when exposed to moisture.[14,21,42] Hence, it still remains a challenge to develop a highly efficient and stable CsPbI$_3$ PSC with a p-i-n structure that is suitable as a top cell for perovskite/Si tandem devices.

During the past few years, MXenes (Ti$_3$C$_2$T$_x$, where T is the surface termination functional group, such as –O, –OH, or –F) or their oxidized forms have been used to modify the electron transport layer (ETL)—or have been used directly as the ETL—in PSCs, mostly focused on n-i-p structures.[43–50] Single-layered MXene nanosheets were used as the ETL to improve Cs$_2$AgBiBr$_6$ double perovskite-based PSCs with more effective electron extraction.[51] The high electron mobility of MXene-based ETL was also shown to enhance the MAPbI$_3$-based PSCs with a high PCE of 18.29%.[48] In another study, MXene was incorporated into a SnO$_2$-MXene nanocomposite as the ETL for MAPbI$_3$ PSCs, and the metallic MXene nanosheets provided efficient charge transfer paths within the ETL, resulting in a high PCE of 18.34%.[43] Later, MXene/single-walled carbon nanotubes (SWCNTs) composites were used to reduce the oxygen vacancy defects of the SnO$_2$ ETL, leading to reduced charge transfer resistance for a high PCE of over 21%.[52] Note that only a few reports centered on p-i-n architectures.[53,54] MXene is generally an excellent conductor, and its conductive properties (e.g., work function) can be intrinsically and widely tuned by simply controlling the degree of oxidation.[55–57] By contrast, other materials such as graphene require additional chemical doping or electrical-field-induced doping in a device configuration and are, therefore, limited in the degree of freedom and relatively less stable.[58] In addition, MXene can passivate surface defects and tune the work function for proper interfacial energy alignment.[44,45,47,49,53,54] Note that most of these studies focused on conventional hybrid perovskites, such as MAPbI$_3$ or mixed-cation-mixed-halide perovskites. Regardless of the device architecture and perovskite composition, controlling the perovskite/MXene interfacial configuration remains a challenge; however, it is critical to device operation.[48,53,54]

Here, a stable CsPbI$_3$-based perovskite layer was formed by spray coating a CsPbI$_3$ precursor on an indium-doped tin oxide (ITO)/poly triarylamine (PTAA) substrate, which was followed by spray coating the mixture of CsPbI$_3$ precursor and preoxidized Ti$_3$C$_2$T$_x$ MXene (OMXene) plates. The sequential spray coating enables the formation of an OMXene-CsPbI$_3$ composite surface layer, which not only offers a protective barrier against moisture ingress but also enhances charge separation from a strong electric field at its interface with the ETL. With this OMXene-based surface engineering approach, the p-i-n-structured CsPbI$_3$/OMXene PSCs reached a PCE of 19.69%. In addition, the encapsulated CsPbI$_3$/OMXene minimodule (25 cm^2), with an initial PCE of 14.64%, showed good stability under simultaneous damp heat (85°C/85% relative humidity [RH]) and 1-sun light soaking for over 1,000 h.

[1]Department of Chemical and Biological Engineering, Korea University, 145 Anam-Ro, Seongbuk-Gu, Seoul 17104, Republic of Korea

[2]Chemistry and Nanoscience Center, National Renewable Energy Laboratory, Golden, CO 80401, USA

[3]Materials Science Center, National Renewable Energy Laboratory, Golden, CO 80401, USA

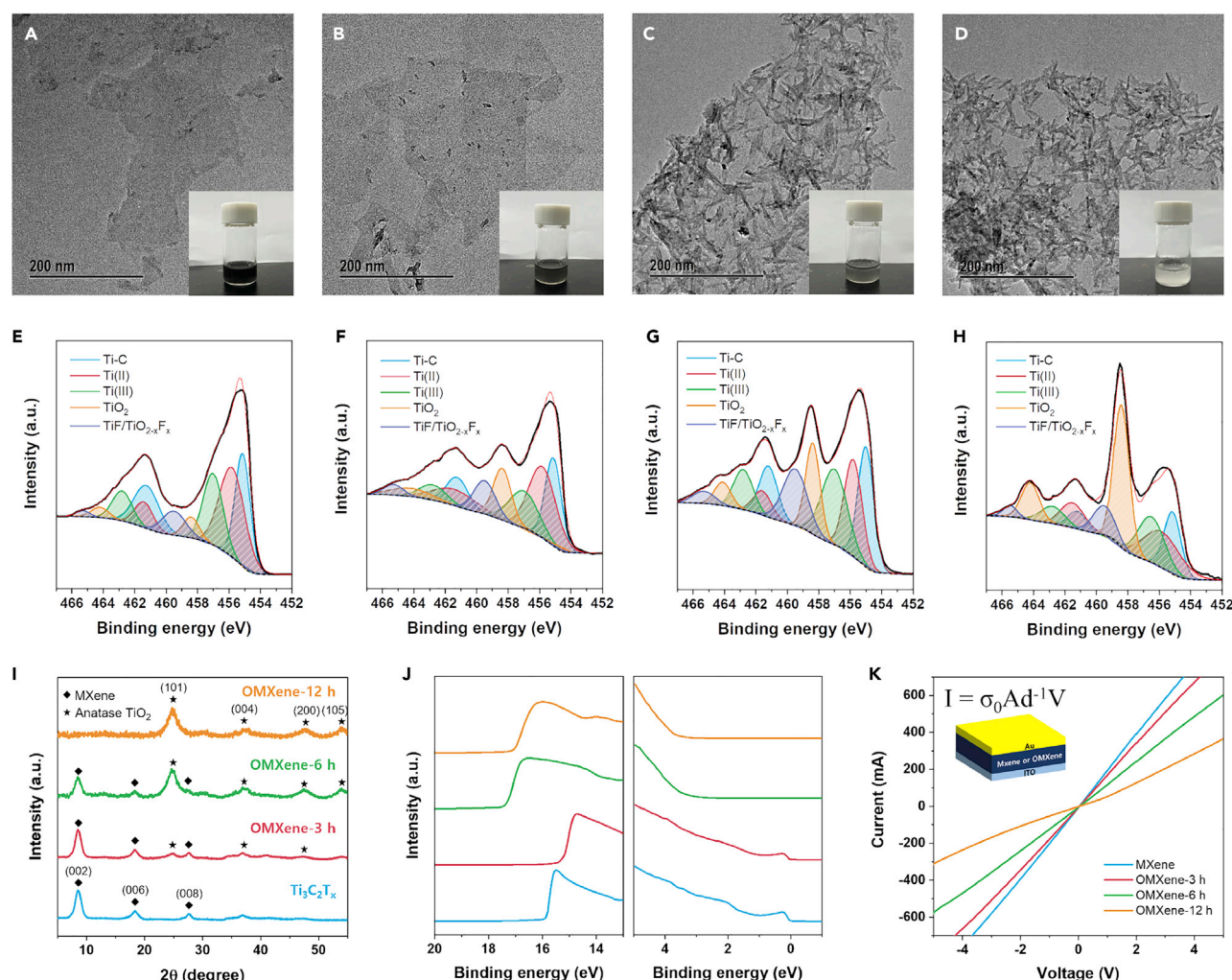[4]Department of Physics, University of Colorado Boulder, Boulder, CO 80309, USA

[5]These authors contributed equally

[6]Present address: School of Chemical Engineering and Technology, Tianjin University, Tianjin 300072, China

[7]Lead contact

*Correspondence: kai.zhu@nrel.gov (K.Z.), imromy@korea.ac.kr (S.H.I.)

https://doi.org/10.1016/j.joule.2022.05.013

Figure 1. Characterization of MXene and OMXene (oxidized MXene)

(A–D) Transmission electron microscopy images of $Ti_3C_2T_x$ MXene (A) and OMXene with oxidation times of 3 h (OMXene-3h: B), 6 h (OMXene-6h: C), and 12 h (OMXene-12h: D).

(E–H) Ti 2p core level X-ray photoelectron spectroscopy spectra of $Ti_3C_2T_x$ MXene (E), OMXene-3h (F), OMXene-6h (G), and OMXene-12h (H).

(I and J) X-ray diffraction patterns (I) and ultraviolet photoelectron spectroscopy spectra (J) of $Ti_3C_2T_x$ MXene, OMXene-3h, OMXene-6h, and OMXene-12h.

(K) Current-voltage characteristics of the ITO/MXene or OMXene/Au devices.

RESULTS AND DISCUSSION

Oxidation control of $Ti_3C_2T_x$ MXene

Figure 1 displays the development and optimization of the electron transporting characteristics of $Ti_3C_2T_x$ MXene with respect to the oxidation reaction time as anatase TiO_2 nanoparticles formed on the surface of the MXene. To obtain MXene, we first purchased commercially available Ti_3AlC_2 MAX (M, early transition metal; A, group 13 and 14 element; X, carbon and/or nitrogen) phase and exfoliated the Al layer by etching according to previously reported procedures.[46] The scanning electron microscopy (SEM) image and X-ray diffraction (XRD) pattern for the commercially available MAX can be seen in Figure S1, and a detailed explanation of how we obtained MXene through MAX exfoliation can be found in the experimental procedures section. We oxidized the exfoliated MXene to form anatase TiO_2 on its surface by dispersing the MXene in H_2O with NaOH and subsequently stirring the

CellPress

Joule
Article

dispersion at 50°C. Transmission electron microscopy (TEM) images of the MXene with respect to the reaction time are shown in Figures 1A–1D. A large nanosheet of MXene was initially observed in Figure 1A, indicating that MXene was well exfoliated from MAX, and an increasing amount of oxidation was observed as the reaction progressed. Nanoparticles had formed on the surface of the MXene after 3 h of reaction (OMXene-3h), as seen in Figure 1B, and a sufficient number of nanoparticles had formed throughout the entire surface of the MXene after 6 h of reaction (OMXene-6h), as seen in Figure 1C. After 12 h of reaction (OMXene-12h), the oxidation appeared to have progressed, as evidenced by the solution color in the inset photograph; consequently, the sheet-like structure of the MXene largely disappeared, as shown in Figure 1D. The insets in each TEM image in Figures 1A–1D are photographs of the actual dispersion at its respective reaction time. Initially, the MXene dispersion exhibits a thick black color, which fades progressively as the reaction proceeds; the dispersion becomes white after 12 h of reaction due to most of the MXene being oxidized.

To determine the changes in chemical composition and bonding due to the oxidation of MXene, we performed X-ray photoelectron spectroscopy (XPS) analyses of the MXene samples with varying reaction times. The Ti 2p XPS spectra of each sample at the reaction times of 0, 3, 6, and 12 h are shown in Figures 1E–1H, respectively, and the corresponding O 1s, C 1s, and F 1s spectra are shown in Figure S2. The Ti 2p core level is fitted with five doublets (Ti 2p 2p$_{3/2}$–Ti 2p$_{1/2}$). The blue peaks at 455.0 eV (461.3 eV) represent the Ti-C species; the pink and green peaks at 455.8 eV (461.4 eV) and 457.0 eV (462.8 eV) represent the Ti (II) and Ti (III) species, respectively; the orange peaks at 458.4 eV (464.2 eV) represent the Ti-O species; and the violet peaks at 459.5 eV (465.3 eV) represent the Ti-F species. As the MXene oxidation progressed with reaction time, changes in chemical bonding and composition were also evident. Initially, the presence of Ti-C species dominated for the pristine unoxidized MXene. The presence of Ti-O species gradually intensified with increasing reaction time due to oxidation, and, eventually, after 12 h of reaction time, it became the dominating signal. Correspondingly, the peak intensity of the TiO$_2$ species at 529.9 eV in the O 1s spectra gradually increased, and the peak intensity of the Ti-C species at 282.2 eV in the C 1s spectrum gradually decreased.[59,60] We can, therefore, infer that the needle-shaped nanoparticles seen in the TEM images are TiO$_2$ formed by the oxidation of MXene. A comparison of the Ti 2p XPS spectrum of the OMXene-12h sample (Figure 1H) and the TiO$_2$ XPS spectrum (Figure S3) reveals high similarities, consistent with the formation of TiO$_2$ from the oxidation of MXene. The remnants of the Ti-C, Ti(II), Ti(III), and Ti-F species are observed in Figure 1H, suggesting that MXene did not fully convert into TiO$_2$ nanoparticles even after 12 h of oxidation, retaining some of its initial chemical structure.

For further identification of the nanoparticles, we analyzed the XRD patterns of each sample, as shown in Figure 1I. Initially, the unoxidized MXene exhibited a strong (002) XRD peak at approximately 9.5°. As the oxidation of MXene progressed with increasing reaction time, a XRD peak at approximately 25.3°, correlating to anatase TiO$_2$, emerged for the OMXene-3h sample, showing a stronger intensity than the MXene (002) peak after 6 h of reaction. The anatase TiO$_2$ peak dominated the XRD pattern for the OMXene-12h sample. The Raman spectra in Figure S4 exhibited the same trend as the TEM/XPS/XRD results and confirmed that the oxidation of MXene progressively induced the formation of anatase TiO$_2$ nanoparticles on the surface of the MXene, eventually causing the disappearance of the sheet-shaped MXene and the formation of needle-shaped anatase TiO$_2$-MXene nanoparticles of approximately 30–50 nm after 12 h of reaction time.[46,48]

Joule
Article

 CellPress

We performed ultraviolet photoelectron spectroscopy (UPS) on each sample and measured their conductivities to characterize the changes in energy levels and conductivities with respect to oxidation time, as presented in Figures 1J and 1K, respectively. From the UPS results (Figure 1J), we confirmed that the pristine unoxidized MXene exhibited metallic behavior with a work function of −5.37 eV. After 3 h of reaction, sparse formation of TiO$_2$ nanoparticles on the surface of the MXene decreased the work function to −6.01 eV while still preserving the metallic characteristics of the MXene. Further oxidation increased the formation of TiO$_2$ nanoparticles, causing the MXene to lose its metallic properties and exhibit semiconductor properties with an energy band gap similar to that of TiO$_2$. We obtained the work function and highest occupied molecular orbital (HOMO) energy level of the OMXene-6h sample, which were −3.91 and −7.39 eV, respectively, and by using the energy band gap of 3.49 eV, we calculated a lowest unoccupied molecular orbital (LUMO) energy level of −3.90 eV. In the case of the fully oxidized OMXene-12h sample, the work function, HOMO, and LUMO energy level values were −4.20, −7.92, and −4.10 eV, respectively. We obtained these values by using the energy band gap of 3.82 eV. The energy band gaps of OMXene-6h and OMXene-12h samples were obtained by Tauc plots from UV spectra, as shown in Figure S5. The energy level diagrams of MXene and OMXene with different oxidations are shown in Figure S6.

We further examined the impact of oxidation time on conductivities via the current-voltage (I-V) measurement of the MXene or OMXene samples sandwiched between ITO and Au, as shown in Figure 1K. The direct current (DC) conductivity can be obtained from the slope of the I-V plot and is given by $I = \sigma_0 A d^{-1} V$, where A is the active area of 0.16 cm^2, d is the active layer thickness, and σ_o is the DC conductivity. The conductivities of the MXene, OMXene-3h, OMXene-6h, and OMXene-12h samples were 23.9, 20.9, 16.9, and 8.0 μS/cm, respectively. The conductivity of OMXene decreased with increasing oxidation because TiO$_2$ particles with low conductivity were formed on the MXene due to oxidation. As a result, although the MXene and OMXene-3h samples exhibit high conductivity, their work functions are too deep to form a good energy band alignment for an efficient solar cell device. The OMXene-12h sample suffers from both bad energy band alignment and low conductivity problems and is also unsuitable as a charge carrier transport layer. Thus, we deemed the OMXene-6h sample to be the most appropriate choice as the charge carrier transport layer for subsequent experiments.

OMXene-CsPbI$_3$ composite surface layer

We investigated the charge carrier transport properties of OMXene-6h by analyzing the photoluminescence (PL) characteristics of the CsPbI$_3$ perovskite film with and without an OMXene-CsPbI$_3$ composite surface layer, as shown in Figure 2. The composite surface layer was formed by spray coating OMXene-CsPbI$_3$ mixed precursor solution on top of the pristine CsPbI$_3$ layer. Figures 2A and 2C are surface SEM images of the CsPbI$_3$ perovskite film without and with OMXene-CsPbI$_3$-composite treatment, respectively. The CsPbI$_3$ perovskite film was formed uniformly, with no pinholes, through spray coating, and the OMXene-CsPbI$_3$ composite-treated film showed a uniform distribution of rod-shaped OMXene nanoplates of 50 nm size throughout the perovskite surface while most OMXene particles in the composite layer can expose their surfaces. The OMXene embedded at an angle might be formed by the preferentially oriented OMXene plates in the sprayed solution drops during the spray coating. Thus, we anticipate that a sufficient number of OMXene particles are in contact with the ETL, leading to an overall positive effect on charge extraction. To investigate the charge carrier transporting properties of OMXene-6h, we took the PL mapping images of the ITO/PTAA/perovskite or perovskite/OMXene-perovskite-composite film
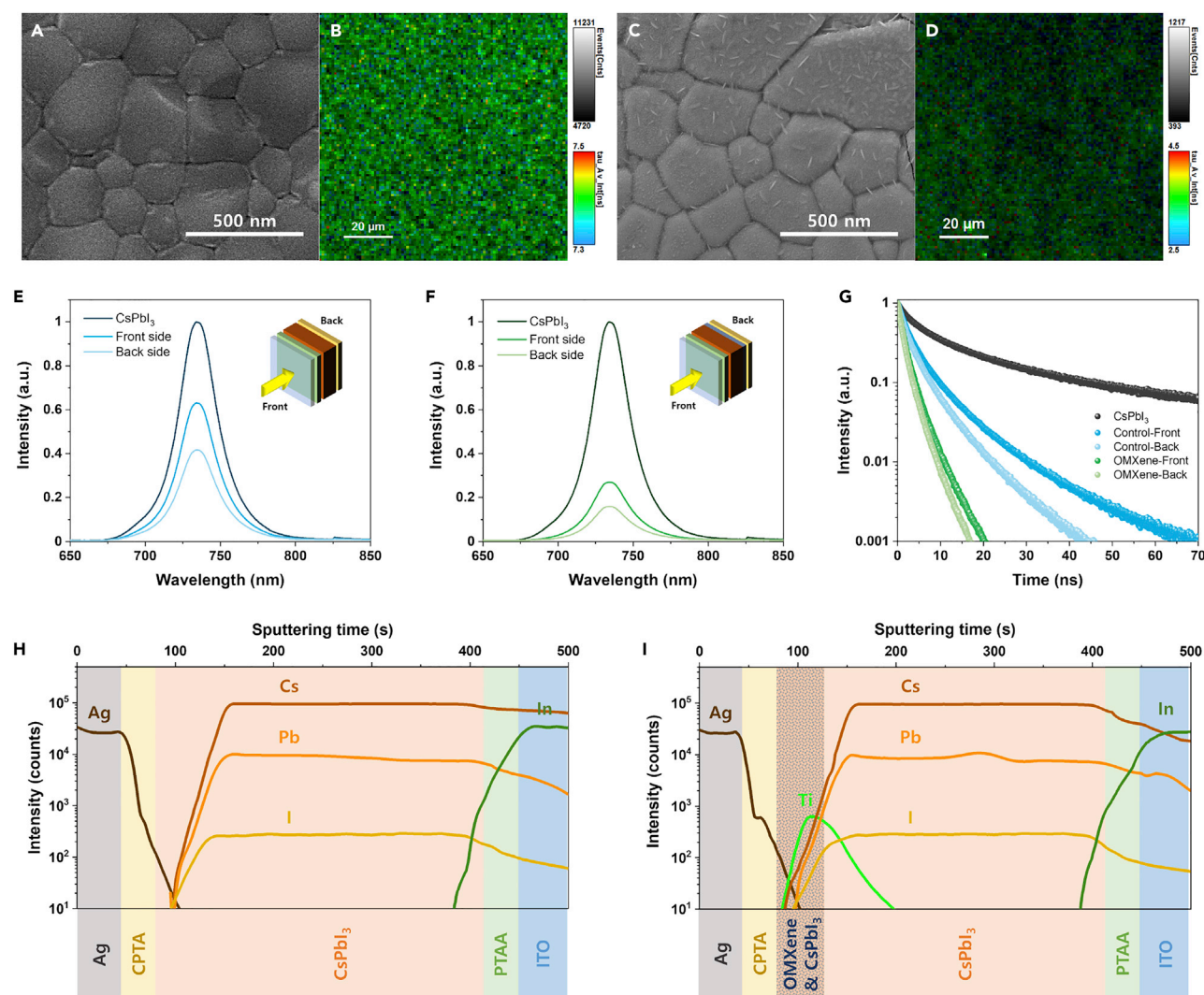
Figure 2. Characterization of CsPbI$_3$ perovskite films without and with OMXene-CsPbI$_3$ composite layer

(A–D) SEM and PL results: (A and C) SEM surface images and (B and D) PL mapping images of the CsPbI$_3$ perovskite films, without (A and B) and with (C and D) OMXene-CsPbI$_3$-composite layer.

(E and F) Static PL spectra of the ITO/PTAA/CsPbI$_3$/CPTA (E) and ITO/PTAA/CsPbI$_3$/OMXene-CsPbI$_3$/CPTA films (F).

(G) Time-resolved PL spectra decay curves of the ITO/PTAA/CsPbI$_3$/CPTA (control) and ITO/PTAA/CsPbI$_3$/OMXene-CsPbI$_3$/CPTA (OMXene) films.

(H and I) Time-of-flight secondary ion mass spectrometry depth profile of the devices without (H) and with (I) OMXene-CsPbI$_3$ composite layer.

surfaces, as presented in Figures 2B and 2D. The PL mapping image of the perovskite film without the OMXene-perovskite composite exhibited a stronger PL intensity than the perovskite film with the OMXene-perovskite composite, and the two samples showed PL lifetimes of approximately 7.4 and 3.5 ns, respectively. The lower PL intensity and shorter PL lifetime in the PL mapping indicates that the charge carriers created in the perovskite layer are quickly transferred/transported through the OMXene-perovskite composite. Thus, the presence of OMXene-CsPbI$_3$ improves charge transport/separation compared with the perovskite-only sample.

We also compared the PL characteristics of the ITO/PTAA/CsPbI$_3$/C$_{60}$ pyrrolidine tris-acid (CPTA) and ITO/PTAA/CsPbI$_3$/OMXene-CsPbI$_3$ composite/CPTA structured samples with respect to different excitation orientations, as shown in Figures 2E and 2F. As expected, the sample passivated with OMXene showed a larger decrease in PL

Joule
Article

CellPress

intensity. In addition, we found that the PL intensity decreased by a larger margin when the PL excitation source entered the samples through the CPTA layer (labeled as "back side") than when the source entered the samples through the ITO substrate (labeled as "front side"). These results suggest that the main junctions of our samples are located at the perovskite/ETL interface as opposed to the PTAA/perovskite interface and further support that the presence of OMXene facilitates charge separation. For the time-resolved photoluminescence (TRPL) measurement in Figure 2G, CsPbI$_3$ film was measured on glass substrate with the excitation from the back side (surface of the film). Since there was no charge transfer within the CsPbI$_3$ film, no significant difference was observed from different excitation direction. The pristine CsPbI$_3$ perovskite film exhibited an average PL lifetime (τ_{avg}) of 10.34 ns. Using the same samples from the PL measurements, the control sample without OMXene-perovskite-composite treatment exhibited τ_{avg} of 4.00 and 3.23 ns as the excitation laser pulse entered the perovskite layer from the front side and back side, respectively. Meanwhile, the OMXene-perovskite-composite-treated sample exhibited τ_{avg} of 1.80 and 1.60 ns for front-side and back-side excitations, respectively. The shorter lifetimes shown by the OMXene-perovskite-composite-treated sample compared with the control sample are attributed to a faster extraction of charge carriers due to the presence of OMXene-perovskite composite, and the shorter lifetimes exhibited from back-side excitations as opposed to front-side excitations indicate that the main junctions of both samples are located at the perovskite/ETL interface, corroborating the results from the static PL measurements.[39,61,62] The TRPL and PL spectra of CsPbI$_3$ and CsPbI$_3$-OMxene-6h film without charge transfer layer are shown in Figure S7.

We also examined the composition depth profiles of both control CsPbI$_3$ and OMXene-6h-treated (CsPbI$_3$/OMXene-CsPbI$_3$ composite) samples in a device stack using time-of-flight secondary ion mass spectrometry (TOF-SIMS), as shown in Figures 2H and 2I. The TOF-SIMS plot for the OMXene-6h sample shows the Ti depth profile penetrating substantially into the bulk perovskite layer from the perovskite/ETL interface and is indicative of the presence of the OMXene-CsPbI$_3$ composite surface layer. This is consistent with the spray coating of the OMXene-CsPbI$_3$ mixed precursor solution on top of the pristine CsPbI$_3$ layer, which forms an OMXene-CsPbI$_3$-composite layer with a decreasing work function at the perovskite/ETL interface. The Ti depth profile obtained from TOF-SIMS analysis is also consistent with the Kelvin probe force microscopy (KPFM) results, which indicate an extended field from the perovskite/ETL interface (Figure 4).

Device characteristics

We then fabricated and evaluated perovskite/OMXene-PSC devices by employing varying concentrations of the OMXene-6h dispersion at 0 wt %, 5 wt %, 10 wt %, and 15 wt %. Figure S8 shows the band-gap structures of OMXene-CsPbI$_3$-composite layers with different concentrations of OMXene-6h through Tauc plots and UPS analysis. Figure S9 shows the corresponding device energy diagram for the full device stack of ITO/PTAA/CsPbI$_3$/OMXene-CsPbI$_3$ composite/CPTA/bathocuproine (BCP)/Ag architecture. As we discussed above, the OMXene-CsPbI$_3$ composite layer can rapidly extract the electrons from the CsPbI$_3$ layer to the ETL. The OMXene-treated layer can also reduce the back flow of electrons from the ETL to the CsPbI$_3$ layer because the formation of TiO$_2$ nanoparticles on the MXene surface exhibits a deep HOMO energy value, ultimately increasing the device PCE. Solar cell characteristics of the control device and the champion device fabricated from OMXene-6h 10 wt % are compared in Figure 3. The current density-voltage (J-V) characteristics of 5 wt % and 15 wt % devices are shown in Figure S10, and a summary of photovoltaic properties for all conditions of OMXene-6h is shown in Table S1. The J-V characteristics of the control device shown in

⟨⟩ CellPress

Joule
Article
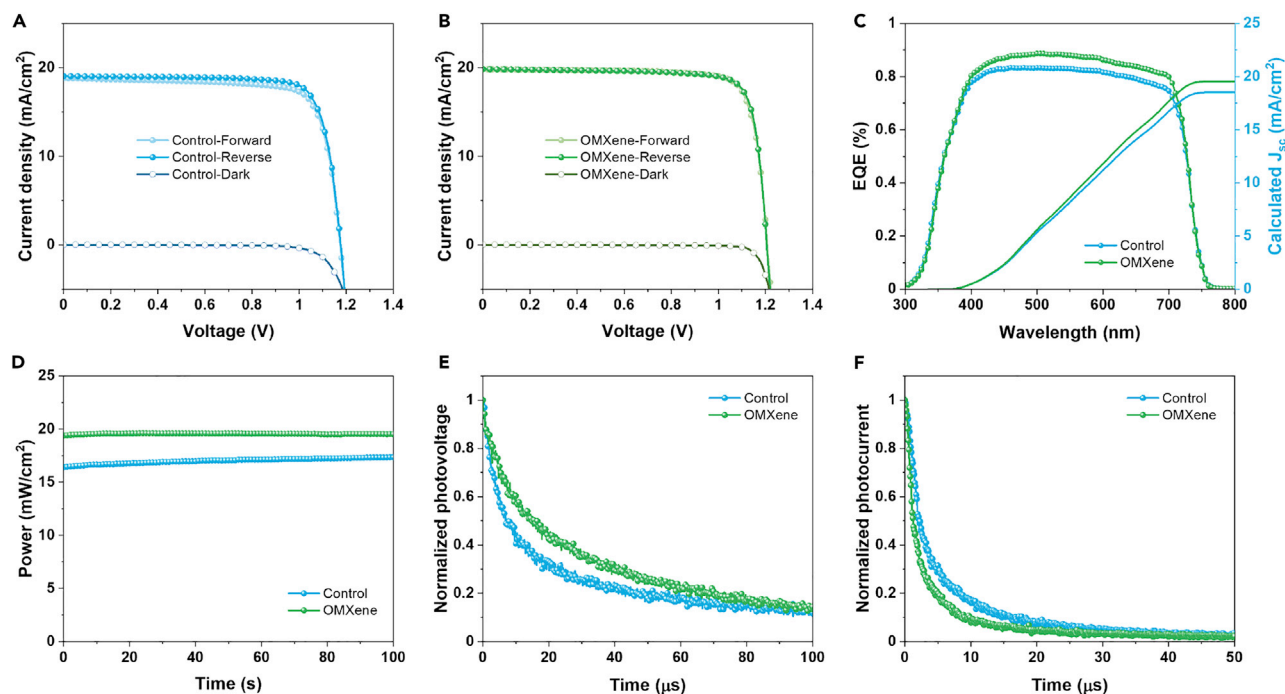
Figure 3. Photovoltaic properties of the CsPbI₃ PSCs without (control) and with OMXene-CsPbI₃ composite layer (OMXene)
(A–C) Current density-voltage curves of the control (A) and OMXene (B) devices, along with their corresponding external quantum efficiency spectra and the integrated current densities (C).
(D–F) Stabilized power output (D), photovoltage decay curve (E), and photocurrent decay curve (F) of the control and OMXene devices.

Figure 3A exhibited an open-circuit voltage (V$_{OC}$) of 1.17 V, short-circuit current density (J$_{SC}$) of 18.81 mA/cm^2, fill factor (FF) of 78.80%, and PCE of 17.35% for the forward scan; a V$_{OC}$ of 1.18 V, J$_{SC}$ of 19.05 mA/cm^2, FF of 80.33%, and PCE of 18.06% for the reverse scan; and average values for V$_{OC}$, J$_{SC}$, FF, and PCE of 1.13 ± 0.04 V, 18.33 ± 0.12 mA/cm^2, 76.10% ± 1.99%, and 15.73% ± 1.01%, respectively, across 30 separate devices. Meanwhile, the device efficiencies of the OMXene-6h devices steadily increased with increasing concentration of the OMXene-6h dispersion, showing peak performance at 10 wt.%, as shown in Figure 3B. The champion device for this condition exhibited a V$_{OC}$ of 1.21 V, J$_{SC}$ of 19.85 mA/cm^2, FF of 81.61%, and PCE of 19.60% for the forward scan; a V$_{OC}$ of 1.21 V, J$_{SC}$ of 19.86 mA/cm^2, FF of 81.96%, and PCE of 19.69% for the reverse scan; and average values for V$_{OC}$, J$_{SC}$, FF, and PCE of 1.16 ± 0.03 V, 19.64 ± 0.23 mA/cm^2, 79.95% ± 1.86%, and 18.22% ± 1.03%, respectively, across 30 separate devices. The box plot comparison of the OMXene-6h treatments with all wt % conditions is shown in Figure S11. The photovoltaic properties of the devices are summarized in Tables 1 and S1. The J-V curves of the champion devices as a function of oxidation time of MXene at concentrations of 5 wt %, 10 wt %, and 15 wt % are shown in Figure S12, and the photovoltaic properties are summarized in Table S2. The external quantum efficiency (EQE) spectra for the control and OMXene-6h devices are shown in Figure 3C; the integrated J$_{SC}$ values are 18.54 and 19.57 mA/cm^2 for the control and OMXene-6h devices, respectively, showing good agreement with the J-V curves. The increase in EQE of the OMXene-6h sample is consistent with the enhanced charge transport/collection associated with the OMXene treatment. In addition, we compared the device performance with spin-coated OMXene layer on top of the perovskite layer, as shown in Figure S13, to check the effectiveness of OMXene-CsPbI₃-composite layers. These devices were clearly worse than the devices coated with the OMXene-CsPbI₃-composite surface

Joule
Article

🝔 **CellPress**

layer (Table S1) despite the general improvement relative to the control devices. Note that the spray coating of OMXene layer on top of perovskite can lead to its easy detachment from the perovskite layer by N_2 flow due to a weak adhesion. These results show the importance of the composite layer approach for enhancing the device performance.

Figure 3D shows the stabilized power outputs of the control and OMXene-6h devices, which were measured for 100 s at their respective maximum power point voltages. The PCE of the control device slowly increased from an initial value of 16.42% to a stabilized value of 17.33% over 100 s, whereas the PCE of the OMXene-6h device barely showed any difference between the initial PCE value of 19.39% and the final value of 19.52%. The OMXene-6h device is quicker to reach its steady-state power output compared with the control device and is also stable enough to maintain a constant power output. For a better understanding of this phenomenon, we measured the transient responses of both devices and plotted their photovoltage decay and photocurrent decay curves in Figures 3E and 3F, respectively. From the photocurrent decay curves in Figure 3F, we found that the decay times of the control and OMXene-6h devices were 2.4 and 1.4 μs, respectively. Transient photocurrent (TPC) measures the charge dynamics within the entire device stack, including charge transport across perovskite and transport layers before the charges are collected or extracted at the contact electrodes. The charge transport process can be slowed down from trap-mediated trapping/detrapping processes. Surface engineering with the composite OMXene layer can enhance charge extraction, suppress charge accumulation (which could impede charge flow), and mitigate the impact of traps/defects on the charge collection/transport process, leading to a faster TPC response. Our observation is also consistent with other reports with MXene-based interfacial modification.[53] On the other hand, the photovoltage decay curves in Figure 3E showed charge carrier recombination lifetimes (τ_{rec}) of 8.2 and 13.8 μs for the control and OMXene-6h devices, respectively. The photocurrent decay curve indicated that transit time (τ_{tr}) decreased when the device was treated with OMXene-6h, whereas the photovoltage decay curve showed that τ_{rec} increased with OMXene-6h treatment. These results agree with a previous study[44] and are consistent with the increase in charge transport/collection efficiency as well as the decrease in charge recombination resulting from the OMXene treatment. In addition, we conducted the space charge limited current (SCLC) analysis of the trap density (N_t) of control and OMXene-6h devices. Lower V_{TFL} was obtained for the electron-only device treated with OMXene in Figure S14. The calculated $N_t = 1.65 \times 10^{15}$ cm^{-3} for OMxene-6h device, while the control device exhibits a higher trap density of $N_t = 2.10 \times 10^{15}$ cm^{-3}. These results suggest that the OMXene-$CsPbI_3$ composite layer contributed to reduced trap density with efficient charge extraction.

To further understand the role of OMXene in increasing device efficiency from the viewpoint of charge separation and charge transport processes, we performed scanning KPFM measurements on the devices with and without OMXene and mapped the electric potential and field distributions in Figure 4. We applied a small bias voltage to induce changes in electric potential throughout the bulk device, mapped the electric potential distribution across the cross-sectional surface of the device at the nanometer scale, and then obtained the changes in the electric field across the cross-sectional surface of the device by taking the first derivative of the electric potential. Figures 4A–4D show the cross-sectional SEM image of the control device, its electric potential profile, the electric potential difference between biased and unbiased samples, and the electric field distribution across the device (obtained by taking the first derivative), respectively, and Figures 4E–4H show the same results for the OMXene-6h device. Under the
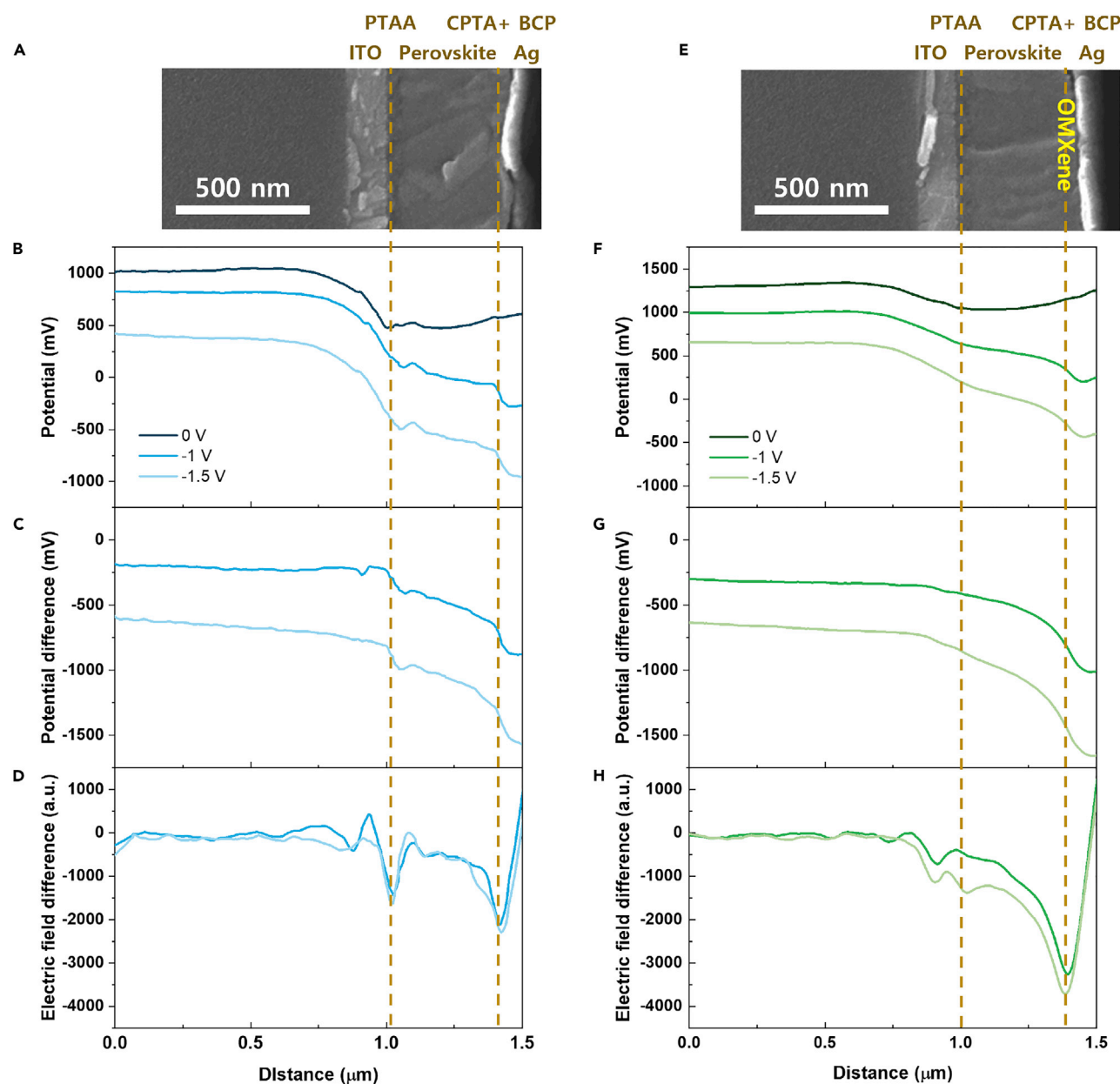
Figure 4. KPFM for electrical potential and field profiling on the cross-sectional surfaces of devices

KPFM results for the control (A–D) and OMXene (E–H) devices. (A and E) SEM cross-sectional images, (B and F) the potential profile under various bias voltages, (C and G) the potential difference under various applied bias voltages relative to that under 0 V, and (D and H) changes in the electric field calculated by taking the first derivatives of the potential difference.

application of reverse bias, Figure 4D reveals two distinct electric fields each at the PTAA/perovskite and perovskite/ETL interfacial p-n junctions of the control device; these two electric fields are comparable, and, thus, neither junction appears to be dominant. By contrast, for the OMXene-6h device shown in Figure 4H, the OMXene-6h/ETL junction at the rear side of the device exhibits a stronger electric field that extends over a wider region, which can facilitate more efficient charge extraction in the device. These results are consistent with the TOF-SIMS comparison shown in Figures 2H–2J, and they support the better device performance of OMXene-treated devices in comparison with pristine devices.
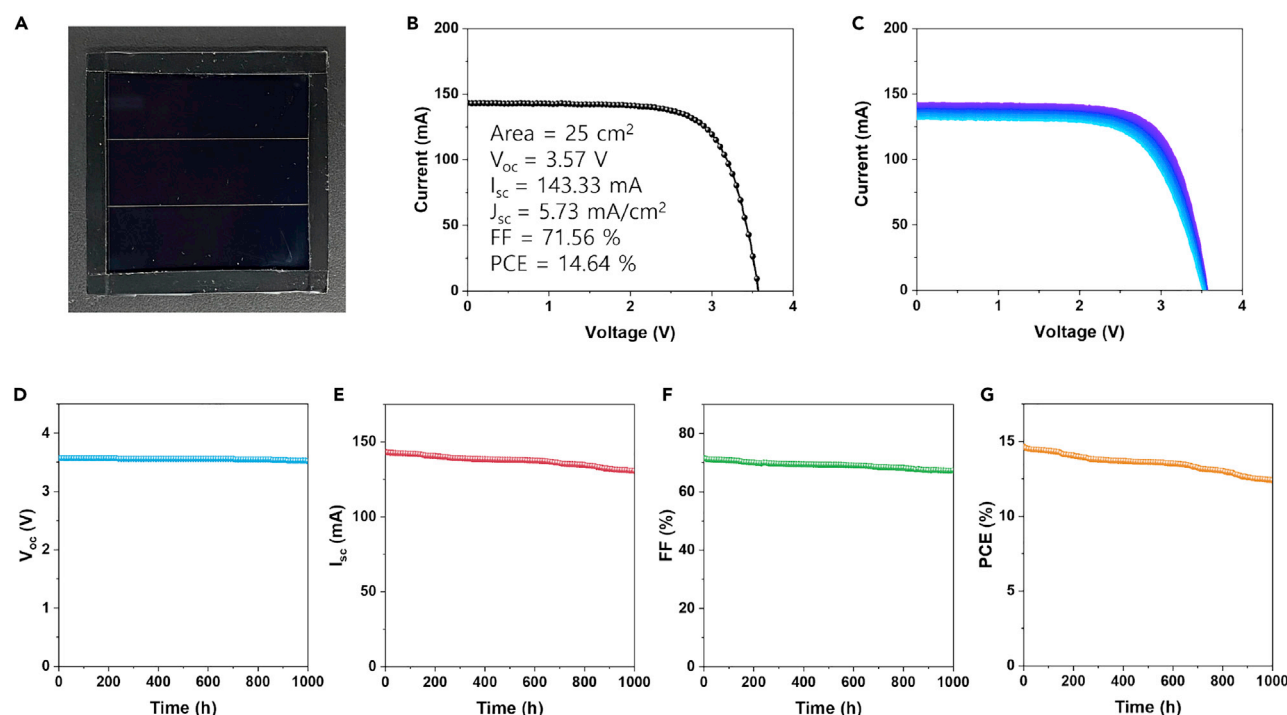
Figure 5. Photovoltaic properties and long-term stability of the CsPbI3 PSC minimodule

(A and B) Photographs (A) and I-V curve (B) of a $CsPbI_3$ perovskite minimodule.

(C–G) Long-term stability test of an encapsulated $CsPbI_3$ perovskite minimodule under simultaneous damp heat (85°C/85% RH) and 1-sun illumination: (C) IV curves from 0 h (violet) to 1,000 h (sky blue) along with the corresponding photovoltaic parameters of V_{oc} (D), I_{sc} (E), FF (F), and PCE (G).

In addition, we measured the V_{oc} dependence on the incident light intensity because it could provide additional useful information regarding recombination in these devices.[63,64] In Figure S15, we compared the V_{oc} dependence on the incident light intensity for the control device and the device with the OMXene-6h modification. The control device showed a slope of 1.54, whereas the OMXene-6h-modified device exhibited a slope of 1.35. In general, the smaller the slope, the less detrimental is the effect of the traps/defects on the device performance.[64] As $CsPbI_3$ is prone to go through phase transition toward inactive delta phase under a humid environment, we believe that the embedded OMXene within $CsPbI_3$/OMXene composite layer can act as a protection barrier against water permeation and, consequently, suppress the formation of defects. Thus, the smaller slope from the OMXene-treated device supports the improved material quality, which is in agreement with our other characterization results such as TRPL, photovoltage decays, KPFM, and device results.

Finally, we fabricated p-i-n-structured inorganic $CsPbI_3$ perovskite minimodules with an aperture area of 25 cm^2, using OMXene-6h to evaluate their I-V performance as well as their stability under rigorous conditions. The p-i-n-structured minimodules were constructed with three individual subcells connected in series, as shown in Figure 5A. The champion minimodule exhibited a V_{OC} of 3.57 V, short-circuit current (I_{SC}) of 143.33 mA, FF of 71.56%, and PCE of 14.64% for the forward scan direction (Figure 5B) and average values for V_{OC}, J_{SC}, FF, and PCE of 3.49 $\pm$ 0.06 V, 5.70 $\pm$ 0.04 mA/cm^2, 65.39% $\pm$ 4.37%, and 13.02% $\pm$ 1.17%, respectively, across 25 separate devices (Figure S16). We plotted the J-V performance distribution across 25 devices in Table 1. The minimodule was then encapsulated with glass and epoxy and

Table 1. Photovoltaic parameters of CsPbI$_3$ PSCs without (control) and with OMXene-CsPbI$_3$ composite layer and of minimodules (area = 25 cm^2) with OMXene-CsPbI$_3$ composite layer

Devices	Scan direction	V_{oc} (V)	J_{sc} (mA/cm^2)	FF (%)	PCE (%)
Control (0 wt %)	forward	1.17	18.81	78.80	17.35
	reverse	1.18	19.05	80.33	18.06
	70 samples	1.13 ± 0.04	18.33 ± 0.31	76.10 ± 1.99	15.73 ± 1.01
OMXene (10 wt %)	forward	1.21	19.85	81.61	19.60
	reverse	1.21	19.86	81.96	19.69
	30 samples	1.16 ± 0.03	19.64 ± 0.23	79.77 ± 1.86	18.22 ± 1.03
Minimodule (5 cm × 5 cm)	forward	3.57	5.73	71.56	14.64
	25 samples	3.49 ± 0.06	5.70 ± 0.04	65.39 ± 4.37	13.02 ± 1.17

stored in a chamber at 85°C/85% RH under 1-sun illumination with a Xenon lamp (modified ISOS-L-3 conditions[65]). The J-V performance of the minimodule was measured every 10 h for over 1,000 h in total, and the J-V curves, as well as the individual parameter performance over time, are plotted in Figures 5C–5G. Before entering the chamber, the minimodule exhibited V_{OC}, J_{SC}, FF, and PCE values of 3.57 V, 5.73 mA/cm^2, 71.52%, and 14.63%, respectively; after 1,000 h, the minimodule exhibited values of 3.52 V, 5.23 mA/cm^2, 67.38%, and 12.40%, respectively, thus retaining ∼85% of its initial PCE. In particular, the minimodule showed extraordinary V_{OC} stability, signifying that the well-matched band alignment of the perovskite layer due to OMXene-perovskite-composite treatment was well maintained throughout the 1,000 h of stability testing.

To further confirm our hypothesis that the OMXene protection layer offers improved stability against moisture, we prepared CsPbI$_3$ and CsPbI$_3$/OMXene films to compare their absorption spectra and XRD patterns over time. Figure S17 is the time evolution of the unencapsulated films over 30 days in N$_2$ at 85°C, and it shows that the CsPbI$_3$ film is resilient against temperature perturbations. Meanwhile, Figure S18 is the time evolution of the unencapsulated films over 60 min at room temperature under 85% RH, and it shows the vulnerability of the CsPbI$_3$ layer to moisture and the effective protection from OMXene. We also compared the long-term stability of CsPbI$_3$ and CsPbI$_3$ with OMXene perovskite minimodules under 1-sun light soaking at 85°C/N$_2$ atmosphere (without encapsulated samples), 25°C/85% RH (without encapsulated samples), and 85°C/85% RH (with encapsulated samples) (Figure S19; Table S3) in order to check whether the OMXene/perovskite composite layer is still effective to the module as a protection layer. The unencapsulated CsPbI$_3$ and CsPbI$_3$ with OMXene perovskite minimodules had good thermal stability under 1-sun light soaking at 85°C/N$_2$ atmosphere as shown in Figures S19A, S19D, S19E, and S19H. However, under 1-sun light soaking at 25°C/85% RH condition, the unencapsulated CsPbI$_3$ sample exhibited a significant performance degradation of 60.1%, whereas the unencapsulated CsPbI$_3$ with OMXene sample had 20.1% of performance degradation, as shown in Figures S19B, S19D, S19F, and S19H. Therefore, the OMXene/perovskite composite layer does not enhance thermal stability but greatly enhances moisture stability, and, consequently, it acts as a protection layer against moisture. Accordingly, the encapsulated CsPbI$_3$ with OMXene minimodule (degradation = 15.2%) had better stability under 1-sun light soaking at 85°C/85% RH condition than the encapsulated CsPbI$_3$ sample (degradation = 24.3%), as shown in Figures S19C, S19D, S19G, and S19H. The remarkable stability in Figure 5 is attributed to the protection effect associated with OMXene. A third-party verification using an IEC 61215 standard damp heat (85°C/85% RH) stability test for 1,000 h for the p-i-n CsPbI$_3$ minimodule with OMXene protection is shown in Figure S20.

Joule
Article

CellPress

Conclusion

In summary, we demonstrated an effective surface engineering technique based on OMXene to significantly improve the efficiency and stability of p-i-n-structured $CsPbI_3$ PSCs. The OMXene-$CsPbI_3$-composite layer was formed via sequential orthogonal spray coating of $CsPbI_3$ and $CsPbI_3$/OMXene precursor solutions. The electronic properties of OMXene were adjusted by controlling MXene oxidation time. The OMXene-6h sample exhibited appropriate HOMO and LUMO values of −7.35 and −3.9 eV, respectively, and a conductivity of 16.9 μS due to the formation of anatase TiO_2 electron transporting shells. The OMXene surface layer facilitates charge carrier extraction, as evidenced by PL mapping, static PL, and TRPL results. These results are further supported by the KPFM measurement, which shows that the OMXene surface treatment strengthens the electric field at the perovskite/ETL interface and broadens the depletion region across the perovskite layer. With the OMXene surface protection approach, we obtained a highly efficient p-i-n $CsPbI_3$ PSC with a V_{OC} of 1.21 V, J_{SC} of 19.86 mA/cm^2, FF of 81.96%, and PCE of 19.69% at the 1-sun condition. In addition, the $CsPbI_3$/OMXene perovskite minimodules with aperture areas of 25 cm^2 exhibited a PCE of 14.64% and good stability under simultaneous damp heat (85°C/85% RH) and 1-sun light soaking for over 1,000 h.

EXPERIMENTAL PROCEDURES

Resource availability

Lead contact

Further information and request for resources and materials should be directed to and will be fulfilled by the lead contact, Sang Hyuk Im (imromy@korea.ac.kr).

Materials availability

This study did not generate new unique materials.

Data and code availability

The data presented in this work are available from the corresponding authors upon reasonable request.

Materials

Cesium iodide (CsI, 99.999%), lead (II) iodide (PbI_2, 99.99%), dimethyl ammonium iodide (DMAI, 98%), lithium fluoride (LiF, 99.99%), CPTA (97%), hydrochloric acid (HCl, 36%), sodium hydroxide (NaOH, ≥98%), dimethylformamide (DMF, 99.8%), *N*-methyl-2-pyrrolidone (NMP, 99.5%), and toluene (99.8%) were purchased from Sigma-Aldrich. 2,9-dimethyl-4,7-diphenyl-1,10-phenanthroline (BCP, >99%) was purchased from Lumtec. Ti_3AlC_2 MAX powder and patterned ITO-coated glass were purchased from 2H.

Preparation of MXene powder and oxidation of MXene

The $Ti_3C_2T_x$ MXene used in this paper was prepared by etching the MAX in a mixture of 12 M LiF and 9 M HCl solution at room temperature for 24 h. Specifically, 1.6 g of LiF was added to 20 mL of 9 M HCl solution at room temperature and stirred for 30 min. Then, 1.0 g of MAX powder was slowly dropped into the etching solution and continuously etched at room temperature for 24 h. After the etching process, the obtained acid mixture was repeatedly washed with deionized water by centrifugation until the pH of the mixture was over 5. Finally, the slurry was placed in ultrasonic bath for 10 min and centrifuged at 3,500 rpm for 1 h. The colloidal supernatant solution with MXene was obtained and then dried under vacuum at 50°C for 24 h. To obtain OMXene, 0.1 g of MXene powder was added to 50 mL of 1 M NaOH aqueous solution and then magnetically stirred vigorously at 50°C for 3 h (OMXene-3h), 6 h

 CellPress

Joule
Article

(OMXene-6h), or 12 h (OMXene-12h). Using an alkaline solution to oxidize MXene was previously reported elsewhere.[66] After the oxidation process, the mixture was repeatedly washed to remove the residual NaOH and recovered by centrifugation. The product was obtained and then fired under vacuum at 50°C for 24 h.

Device fabrication

The patterned ITO-coated glass substrates were cleaned by ultrasonication in deionized water, acetone, and isopropanol for 15 min, sequentially, and then dried and treated with argon plasma for 1 min. The PTAA solution (5 mg/mL in toluene) was spin coated on an ITO glass substrate at 6,000 rpm for 30 s, which was followed by thermal annealing on a hot plate at 100°C for 10 min. The 0.25-M CsPbI$_3$ perovskite spray-coating precursor solution was prepared by dissolving 0.65 g of CsI, 1.15 g of PbI$_2$, and 0.43 g of DMAI in 10 mL of a mixed solvent system (DMF:NMP = 8.5:1.5 volume ratio). To prepare the spray-coating precursor solution of the OMXene-CsPbI$_3$-perovskite composite, the 0.20-M CsPbI$_3$ perovskite solution was prepared by dissolving 0.52 g of CsI, 0.92 g of PbI$_2$, and 0.35 g of DMAI in 10 mL of the mixed solvent above, and then, 5 wt % (0.08 g), 10 wt % (0.16 g), and 15 wt % (0.25 g) of OMXene powder, based on the weight of the dissolved CsPbI$_3$ perovskite in solvent, were mixed into the perovskite solution, respectively. The OMXene-CsPbI$_3$-perovskite-composite thin film was prepared on the PTAA/ITO substrate by sequentially spray coating the CsPbI$_3$ perovskite precursor solution followed by the OMXene-CsPbI$_3$-perovskite composition precursor solution. The spray coating was conducted using an ultrasonic spray coater (S80, CERA-TORQ, 80 kHz) combined with a 3D printer (CREALITY, CR-10S PRO), where the perovskite spray-coating precursor solution was delivered by a syringe pump (KD-Scientific, KDS100). The conditions for the ultrasonic spray-coating process are as follows: a nozzle-to-substrate distance of 5 cm, nozzle scan rate of 5 mm/s, solution flow rate of 0.5 mL/min (flow gas: N$_2$/pressure: 7 psi), and deposition temperature of 170°C. After spraying the perovskite solution, the substrate was annealed at 150°C for 10 min. The amount of DMA$^+$ in the final perovskite film was estimated to be less than 2%. Finally, 30-nm CPTA, 10-nm BCP, and 100-nm Ag were sequentially deposited by thermal evaporation at <10^{-5} Torr with deposition rates of 0.5, 0.2, and 2 Å/s, respectively. For device encapsulation, we covered the device active area with glass and sealed the edges with epoxy resin. All device fabrication processes except for thermal evaporation were performed at 25°C and 20% RH under air atmosphere.

Characterization

Morphological images of MXene and OMXene nanosheets were obtained using a field emission TEM (K-Alpha, Thermo Electron). XRD patterns of MXene and OMXene powder were measured by an XRD machine (D8 Advance, Bruker) with a radiation source of Cu-K$_\alpha$ line (λ = 1.5412Å). The ultraviolet-visible (UV-vis) spectra of MXene and OMXene colloidal solutions were measured using an UV-vis-near-infrared (NIR) spectrometer (UV-3600 Plus, Shimadzu). The chemical composition and bonding of MXene and OMXene were obtained by an XPS machine (K-Alpha/Thermo Electron) with an Ar ion gun. The UPS spectra of MXene and OMXene thin films were measured using a photoelectron spectrometer (ESCALAB 250Xi, Thermo Scientific) with He I radiation (21.2 eV). TRPL mappings of perovskite thin films with and without OMXene were obtained by a TRPL measurement system (FluoTime300, PicoQuant). The EQE was measured by a power source (150 W Xenon lamp, 13014, Abet Technologies) with a monochromator (MonoRa-500i, DongWoo Optron) and potentiostat (IviumStat, Ivium). J-V curves were measured by a solar simulator (Sun 3000 Solar Simulator, Abet Technologies) with a source meter (Keithley 2420, Keithley) under the illumination of 1 sun (100 mW/cm^2 AM 1.5G), which was calibrated by a certified Si-reference cell. The J-V curves were measured by masking the active area with a metal mask that had an

Joule
Article

CellPress

aperture area of 0.096 cm^2. KPFM measurements were performed on an atomic force microscope (Autoshot, Nanofocus) inside an Ar-filled glovebox via a Pt/Ir-coating on tip (PPP-EFM-50, NANOSENSORS). The scans have a spatial resolution of ∼70 nm and an electrical resolution of 10 mV. Cross-sectional samples were prepared inside the glovebox without exposure to air; no polishing or ion-milling treatment was involved. During the measurement, we applied bias voltages to the whole-cell stack, and KPFM mapped the cross-sectional surface in dark conditions. For the stability measurement, we placed the encapsulated samples in a simultaneous damp heat (85°C/ 85% RH) chamber and conducted 1-sun light soaking for over 1,000 h.

SUPPLEMENTAL INFORMATION

ACKNOWLEDGMENTS

AUTHOR CONTRIBUTIONS

S.H.I. and K.Z. supervised the research. J.H.H. and F.Z. designed the experiments, carried out the experimental study on device fabrication, and performed basic characterization. D.S.L. performed PL and TRPL measurements. J.K.P. performed XPS and UPS measurements. S.J.H. performed XRD characterizations and analyzed the data. J.M.L. and J.J.B. provided valuable contributions to the experimental results discussion and manuscript preparation. J.H.H., D.S.L., K.Z., and S.H.I. wrote the draft of the manuscript. All the authors made a substantial contribution to the discussion of the content and reviewed and edited the manuscript before submission.

DECLARATION OF INTERESTS

The authors declare no competing interests.

🔗 **CellPress**

Joule
Article

REFERENCES

1. Kojima, A., Teshima, K., Shirai, Y., and Miyasaka, T. (2009). Organometal halide perovskites as visible-light sensitizers for photovoltaic cells. J. Am. Chem. Soc. *131*, 6050–6051.

2. National Renewable Energy Laboratory (2022). Best research-cell efficiency chart. https://www.nrel.gov/pv/cell-efficiency.html.

3. Li, M., Li, H., Fu, J., Liang, T., and Ma, W. (2020). Recent progress on the stability of perovskite solar cells in a humid environment. J. Phys. Chem. C *124*, 27251–27266.

4. Meng, L., You, J., and Yang, Y. (2018). Addressing the stability issue of perovskite solar cells for commercial applications. Nat. Commun. *9*, 5265.

5. Wang, R., Mujahid, M., Duan, Y., Wang, Z.-K., Xue, J., and Yang, Y. (2019). A review of perovskites solar cell stability. Adv. Funct. Mater. *29*, 1808843.

6. Wang, Z., Shi, Z., Li, T., Chen, Y., and Huang, W. (2017). Stability of perovskite solar cells: a prospective on the substitution of the A cation and X anion. Angew. Chem. Int. Ed. Engl. *56*, 1190–1212.

7. Zhou, Y., and Zhao, Y. (2019). Chemical stability and instability of inorganic halide perovskites. Energy Environ. Sci. *12*, 1495–1511.

8. Xiang, W., and Tress, W. (2019). Review on recent progress of all-inorganic metal halide perovskites and solar cells. Adv. Mater. *31*, e1902851.

9. Tian, J., Xue, Q., Yao, Q., Li, N., Brabec, C.J., and Yip, H.-L. (2020). Inorganic halide perovskite solar cells: progress and challenges. Adv. Energy Mater. *10*, 2000183.

10. Tai, Q., Tang, K.-C., and Yan, F. (2019). Recent progress of inorganic perovskite solar cells. Energy Environ. Sci. *12*, 2375–2405.

11. Liang, J., and Qi, Y.B. (2021). Recent progress on all-inorganic metal halide perovskite solar cells. Mater. Today Nano *16*, 100143.

12. Montecucco, R., Quadrivi, E., Po, R., and Grancini, G. (2021). All-inorganic cesium-based hybrid perovskites for efficient and stable solar cells and modules. Adv. Energy Mater. *11*, 2100672.

13. Heo, J.H., Zhang, F., Xiao, C., Heo, S.J., Park, J.K., Berry, J.J., Zhu, K., and Im, S.H. (2021). Efficient and stable graded CsPbI₃₋ₓBrₓ perovskite solar cells and submodules by orthogonal processable spray coating. Joule *5*, 481–494.

14. Sutton, R.J., Eperon, G.E., Miranda, L., Parrott, E.S., Kamino, B.A., Patel, J.B., Hörantner, M.T., Johnston, M.B., Haghighirad, A.A., Moore, D.T., and Snaith, H.J. (2016). Bandgap-tunable cesium lead halide perovskites with high thermal stability for efficient solar cells. Adv. Energy Mater. *6*, 1502458.

15. Nam, J.K., Jung, M.S., Chai, S.U., Choi, Y.J., Kim, D., and Park, J.H. (2017). Unveiling the crystal formation of cesium lead mixed-halide perovskites for efficient and stable solar cells. J. Phys. Chem. Lett. *8*, 2936–2940.

16. Yin, G., Zhao, H., Jiang, H., Yuan, S., Niu, T., Zhao, K., Liu, Z., and Liu, S.F. (2018). Precursor engineering for all-inorganic CsPbI₂Br perovskite solar cells with 14.78% efficiency. Adv. Funct. Mater. *28*, 1803269.

17. Bai, D., Bian, H., Jin, Z., Wang, H., Meng, L., Wang, Q., and Liu, S. (2018). Temperature-assisted crystallization for inorganic CsPbI₂Br perovskite solar cells to attain high stabilized efficiency 14.81%. Nano Energy *52*, 408–415.

18. Kim, D.H., Heo, J.H., and Im, S.H. (2019). Hysteresis-less CsPbI₂Br mesoscopic perovskite solar cells with a high open-circuit voltage exceeding 1.3 V and 14.86% of power conversion efficiency. ACS Appl. Mater. Interfaces *11*, 19123–19131.

19. Heo, J.H., Kim, D.H., Park, J.K., Choi, Y.K., Lee, D.S., and Im, S.H. (2019). Thermally stable inorganic CsPbI₂Br mesoscopic metal halide perovskite solar submodules. ACS Appl. Mater. Interfaces *11*, 43066–43074.

20. Bian, H., Bai, D., Jin, Z., Wang, K., Liang, L., Wang, H., Zhang, J., Wang, Q., and Liu, S. (2018). Graded bandgap CsPbI₂₊ₓBr₁₋ₓ perovskite solar cells with a stabilized efficiency of 14.4%. Joule *2*, 1500–1510.

21. Wang, Y., Dar, M.I., Ono, L.K., Zhang, T., Kan, M., Li, Y., Zhang, L., Wang, X., Yang, Y., Gao, X., et al. (2019). Thermodynamically stabilized β-CsPbI₃-based perovskite solar cells with efficiencies >18%. Science *365*, 591–595.

22. Wang, Y., Liu, X., Zhang, T., Wang, X., Kan, M., Shi, J., and Zhao, Y. (2019). The role of dimethylammonium iodide in CsPbI₃ perovskite fabrication: additive or dopant? Angew. Chem. Int. Ed. Engl. *58*, 16691–16696.

23. Yoon, S.M., Min, H., Kim, J.B., Kim, G., Lee, K.S., and Seok, S.I. (2021). Surface engineering of ambient-air-processed cesium lead triiodide layers for efficient solar cells. Joule *5*, 183–196.

24. Swarnkar, A., Marshall, A.R., Sanehira, E.M., Chernomordik, B.D., Moore, D.T., Christians, J.A., Chakrabarti, T., and Luther, J.M. (2016). Quantum dot-induced phase stabilization of α-CsPbI₃ perovskite for high-efficiency photovoltaics. Science *354*, 92–95.

25. Xue, J., Wang, R., Wang, K.-L., Wang, Z.-K., Yavuz, I., Wang, Y., Yang, Y., Gao, X., Huang, T., Nuryyeva, S., et al. (2019). Crystalline liquid-like behavior: surface-induced secondary grain growth of photovoltaic perovskite thin film. J. Am. Chem. Soc. *141*, 13948–13953.

26. Tan, S., Yu, B., Cui, Y., Meng, F., Huang, C., Li, Y., Chen, Z., Wu, H., Shi, J., Luo, Y., et al. (2022). Temperature-reliable low-dimensional perovskites passivated black-phase CsPbI₃ toward stable and efficient photovoltaics. Angew. Chem. Int. Ed. Engl. e202201300.

27. Bush, K.A., Palmstrom, A.F., Yu, Z.J., Boccard, M., Cheacharoen, R., Mailoa, J.P., McMeekin, D.P., Hoye, R.L.Z., Bailie, C.D., Leijtens, T., et al. (2017). 23.6%-efficient monolithic perovskite/silicon tandem solar cells with improved stability. Nat. Energy *2*, 17009.

28. Bush, K.A., Manzoor, S., Frohna, K., Yu, Z.J., Raiford, J.A., Palmstrom, A.F., Wang, H.-P., Prasanna, R., Bent, S.F., Holman, Z.C., and McGehee, M.D. (2018). Minimizing current and voltage losses to reach 25% efficient monolithic two-terminal perovskite–silicon tandem solar cells. ACS Energy Lett. *3*, 2173–2180.

29. Sahli, F., Werner, J., Kamino, B.A., Bräuninger, M., Monnard, R., Paviet-Salomon, B., Barraud, L., Ding, L., Diaz Leon, J.J., Sacchetto, D., et al. (2018). Fully textured monolithic perovskite/silicon tandem solar cells with 25.2% power conversion efficiency. Nat. Mater. *17*, 820–826.

30. Mazzarella, L., Lin, Y.-H., Kirner, S., Morales-Vilches, A.B., Korte, L., Albrecht, S., Crossland, E., Stannowski, B., Case, C., Snaith, H.J., and Schlatmann, R. (2019). Infrared light management using a nanocrystalline silicon oxide interlayer in monolithic perovskite/silicon heterojunction tandem solar cells with efficiency above 25%. Adv. Energy Mater. *9*, 1803241.

31. Jošt, M., Köhnen, E., Morales-Vilches, A.B., Lipovšek, B., Jäger, K., Macco, B., Al-Ashouri, A., Krč, J., Korte, L., Rech, B., et al. (2018). Textured interfaces in monolithic perovskite/silicon tandem solar cells: advanced light management for improved efficiency and energy yield. Energy Environ. Sci. *11*, 3511–3523.

32. Chen, B., Yu, Z.J., Manzoor, S., Wang, S., Weigand, W., Yu, Z., Yang, G., Ni, Z., Dai, X., Holman, Z.C., and Huang, J. (2020). Blade-coated perovskites on textured silicon for 26%-efficient monolithic perovskite/silicon tandem solar cells. Joule *4*, 850–864.

33. Hou, Y., Aydin, E., De Bastiani, M.D., Xiao, C., Isikgor, F.H., Xue, D.-J., Chen, B., Chen, H., Bahrami, B., Chowdhury, A.H., et al. (2020). Efficient tandem solar cells with solution-processed perovskite on textured crystalline silicon. Science *367*, 1135–1140.

34. Kim, D., Jung, H.J., Park, I.J., Larson, B.W., Dunfield, S.P., Xiao, C., Kim, J., Tong, J., Boonmongkolras, P., Ji, S.G., et al. (2020). Efficient, stable silicon tandem cells enabled by anion-engineered wide-bandgap perovskites. Science *368*, 155–160.

35. Lamanna, E., Matteocci, F., Calabrò, E., Serenelli, L., Salza, E., Martini, L., Menchini, F., Izzi, M., Agresti, A., Pescetelli, S., et al. (2020). Mechanically stacked, two-terminal graphene-based perovskite/silicon tandem solar cell with efficiency over 26%. Joule *4*, 865–881.

36. Xu, J., Boyd, C.C., Yu, Z.J., Palmstrom, A.F., Witter, D.J., Larson, B.W., France, R.M., Werner, J., Harvey, S.P., Wolf, E.J., et al. (2020). Triple-halide wide-band gap perovskites with suppressed phase segregation for efficient tandems. Science *367*, 1097–1104.

37. Wang, R., Huang, T., Xue, J., Tong, J., Zhu, K., and Yang, Y. (2021). Prospects for metal halide perovskite-based tandem solar cells. Nat. Photonics *15*, 411–425.

38. Kottokkaran, R., Gaonkar, H.A., Bagheri, B., and Dalal, V.L. (2018). Efficient p-i-n inorganic CsPbI₃ perovskite solar cell deposited using layer-by-layer vacuum deposition. J. Vac. Sci. Technol. A *36*, 041201.

39. Wang, J., Zhang, J., Zhou, Y., Liu, H., Xue, Q., Li, X., Chueh, C.-C., Yip, H.-L., Zhu, Z., and Jen,

Joule
Article

A.K.Y. (2020). Highly efficient all-inorganic perovskite solar cells with suppressed non-radiative recombination by a Lewis base. Nat. Commun. *11*, 177.

40. Fu, S., Wan, L., Zhang, W., Li, X., Song, W., and Fang, J. (2020). Tailoring in situ healing and stabilizing post-treatment agent for high-performance inverted CsPbI$_3$ perovskite solar cells with efficiency of 16.67%. ACS Energy Lett. *5*, 3314–3321.

41. Fu, S., Li, X., Wan, J., Zhang, W., Song, W., and Fang, J. (2021). In situ stabilized CsPbI$_3$ for air-fabricated inverted inorganic perovskite pho-tovoltaics with wide humidity operating win-dow. Adv. Funct. Mater. *32*, 2111116.

42. Marronnier, A., Roma, G., Boyer-Richard, S., Pedesseau, L., Jancu, J.-M., Bonnassieux, Y., Katan, C., Stoumpos, C.C., Kanatzidis, M.G., and Even, J. (2018). Anharmonicity and disorder in the black phases of cesium lead iodide used for stable inorganic perovskite solar cells. ACS Nano *12*, 3477–3486.

43. Yang, L., Dall'Agnese, Y., Hantanasirisakul, K., Shuck, C.E., Maleski, K., Alhabeb, M., Chen, G., Gao, Y., Sanehira, Y., Jena, A.K., et al. (2019). SnO$_2$–Ti$_3$C$_2$ MXene electron transport layers for perovskite solar cells. J. Mater. Chem. A *7*, 5635–5642.

44. Agresti, A., Pazniak, A., Pescetelli, S., Di Vito, A., Rossi, D., Pecchia, A., Auf der Maur, M.A., Liedl, A., Larciprete, R., Kuznetsov, D.V., et al. (2019). Titanium-carbide MXenes for work function and interface engineering in perovskite solar cells. Nat. Mater. *18*, 1228–1234.

45. Chen, T., Tong, G., Xu, E., Li, H., Li, P., Zhu, Z., Tang, J., Qi, Y., and Jiang, Y. (2019). Accelerating hole extraction by inserting 2D Ti$_3$C$_2$-MXene interlayer to all inorganic perov-skite solar cells with long-term stability. J. Mater. Chem. A *7*, 20597–20603.

46. Yang, L., Dall'Agnese, C., Dall'Agnese, Y., Chen, G., Gao, Y., Sanehira, Y., Jena, A.K., Wang, X.-F., Gogotsi, Y., and Miyasaka, T. (2019). Surface-modified metallic Ti$_3$C$_2$T$_x$ MXene as electron transport layer for planar heterojunction perovskite solar cells. Adv. Funct. Mater. *29*, 1905694.

47. Wang, Y., Xiang, P., Ren, A., Lai, H., Zhang, Z., Xuan, Z., Wan, Z., Zhang, J., Hao, X., Wu, L., et al. (2020). MXene-modulated electrode/SnO$_2$ interface boosting charge transport in perovskite solar cells. ACS Appl. Mater. Interfaces *12*, 53973–53983.

48. Yang, L., Kan, D., Dall'Agnese, C., Dall'Agnese, Y., Wang, B., Jena, A.K., Wei, Y., Chen, G., Wang, X.-F., Gogotsi, Y., and Miyasaka, T. (2021). Performance improvement of MXene-based perovskite solar cells upon property transition from metallic to semiconductive by oxidation of Ti$_3$C$_2$T$_x$ in air. J. Mater. Chem. A *9*, 5016–5025.

49. Wang, J., Cai, Z., Lin, D., Chen, K., Zhao, L., Xie, F., Su, R., Xie, W., Liu, P., and Zhu, R. (2021). Plasma oxidized Ti$_3$C$_2$T$_x$ MXene as electron transport layer for efficient perovskite solar cells. ACS Appl. Mater. Interfaces *13*, 32495–32502.

50. Yang, L., Wang, B., Dall'Agnese, C., Dall'Agnese, Y., Chen, G., Jena, A.K., Wang, X.-F., and Miyasaka, T. (2021). Hybridization of SnO$_2$ and an in-situ-oxidized Ti$_3$C$_2$T$_x$ MXene electron transport bilayer for high-perfor-mance planar perovskite solar cells. ACS Sustainable Chem. Eng. *9*, 13672–13680.

51. Li, Z., Wang, P., Ma, C., Igbari, F., Kang, Y., Wang, K.-L., Song, W., Dong, C., Li, Y., Yao, J., et al. (2021). Single-layered MXene nanosheets doping TiO$_2$ for efficient and stable double perovskite solar cells. J. Am. Chem. Soc. *143*, 2593–2600.

52. Bati, A.S.R., Hao, M., Macdonald, T.J., Batmunkh, M., Yamauchi, Y., Wang, L., and Shapter, J.G. (2021). 1D-2D synergistic MXene-nanotubes hybrids for efficient perovskite solar cells. Small *17*, e2101925.

53. Saranin, D., Pescetelli, S., Pazniak, A., Rossi, D., Liedl, A., Yakusheva, A., Luchnikov, L., Podgorny, D., Gostischev, P., Didenko, S., et al. (2021). Transition metal carbides (MXenes) for efficient NiO-based inverted perovskite solar cells. Nano Energy *82*, 105771.

54. Chava, V.S.N., Chandrasekhar, P.S., Gomez, A., Echegoyen, L., and Sreenivasan, S.T. (2021). MXene-based tailoring of carrier dynamics, defect passivation, and interfacial band alignment for efficient planar p–i–n perovskite solar cells. ACS Appl. Energy Mater. *4*, 12137–12148.

55. Naguib, M., Kurtoglu, M., Presser, V., Lu, J., Niu, J., Heon, M., Hultman, L., Gogotsi, Y., and Barsoum, M.W. (2011). Two-dimensional nanocrystals produced by exfoliation of Ti$_3$AlC$_2$. Adv. Mater. *23*, 4248–4253.

56. Chertopalov, S., and Mochalin, V.N. (2018). Environment-sensitive photoresponse of spontaneously partially oxidized Ti$_3$C$_2$ MXene thin films. ACS Nano *12*, 6109–6116.

57. Pazniak, H., Plugin, I.A., Loes, M.J., Inerbaev, T.M., Burmistrov, I.N., Gorshenkov, M., Polcak, J., Varezhnikov, A.S., Sommer, M., Kuznetsov, D.V., et al. (2020). Partially oxidized Ti$_3$C$_2$T$_x$ MXenes for fast and selective detection of organic vapors at part-per-million concentra-tions. ACS Appl. Nano Mater. *3*, 3195–3204.

58. Yu, Y.-J., Zhao, Y., Ryu, S., Brus, L.E., Kim, K.S., and Kim, P. (2009). Tuning the graphene work function by electric field effect. Nano Lett. *9*, 3430–3434.

59. Agresti, A., Pazniak, A., Pescetelli, S., Di Vito, A., Rossi, D., Pecchia, A., Auf der Maur, M., Liedl, A., Larciprete, R., Kuznetsov, D.V., et al. (2019). Titanium-carbide MXenes for work function and interface engineering in perovskite solar cells. Nat. Mater. *18*, 1228–1234.

60. Shah, S.A., Habib, T., Gao, H., Gao, P., Sun, W., Green, M.J., and Radovic, M. (2016). Template-free 3D titanium carbide (Ti$_3$C$_2$T$_x$) MXene particles crumpled by capillary forces. Chem. Commun. (Camb) *53*, 400–403.

61. Zuo, L., Guo, H., deQuilettes, D.W., Jariwala, S., De Marco, N.D., Dong, S., DeBlock, R., Ginger, D.S., Dunn, B., Wang, M., and Yang, Y. (2017). Polymer-modified halide perovskite films for efficient and stable planar heterojunction solar cells. Sci. Adv. *3*, e1700106.

62. Tan, F., Saidaminov, M.I., Tan, H., Fan, J.Z., Wang, Y., Yue, S., Wang, X., Shen, Z., Li, S., Kim, J., et al. (2020). Dual coordination of Ti and Pb using bilinkable ligands improves perovskite solar cell performance and stability. Adv. Funct. Mater. *30*, 2005155.

63. Yu, B., Shi, J., Tan, S., Cui, Y., Zhao, W., Wu, H., Luo, Y., Li, D., and Meng, Q. (2021). Efficient (>20%) and stable all-inorganic cesium lead triiodide solar cell enabled by thiocyanate molten salts. Angew. Chem. Int. Ed. Engl. *60*, 13436–13443.

64. Zheng, Y., Yang, X., Su, R., Wu, P., Gong, Q., and Zhu, R. (2020). High-performance CsPbI$_x$Br$_{3-x}$ all-inorganic perovskite solar cells with efficiency over 18% via spontaneous interfacial manipulation. Adv. Funct. Mater. *30*, 2000457.

65. Khenkin, M.V., Katz, E.A., Abate, A., Bardizza, G., Berry, J.J., Brabec, C., Brunetti, F., Bulović, V., Burlingame, Q., Di Carlo, A., et al. (2020). Consensus statement for stability assessment and reporting for perovskite photovoltaics based on ISOS procedures. Nat. Energy *5*, 35–49.

66. Dall'Agnese, Y., Lukatskaya, M.R., Cook, K.M., Taberna, P.-L., Gogotsi, Y., and Simon, P. (2014). High capacitance of surface-modified 2D titanium carbide in acidic electrolyte. Electrochem. Commun. *48*, 118–122.